Journal of
Chemical Engineering & Process Technology

Gradov et al., J Chem Eng Process Technol 2017, 8:3
DOI: 10.4172/2157-7048.1000348

Research Article Open Access

Experimental and Numerical Study of Multiphase Mixing Hydrodynamics in Batch Stirred Tank Applied to Ammoniacal Thiosulphate Leaching of Gold

Dmitry Vladimirovich Gradov[1]*, Gerardo González[2], Marko Vauhkonen[2], Arto Laari[1] and Tuomas Koiranen[1]

[1]School of Engineering Science, Lappeenranta University of Technology, Lappeenranta, Finland
[2]Department of Applied Physics, University of Eastern Finland, Kuopio, Finland

Abstract

Hydrodynamics of aerated slurry is studied experimentally and numerically using the example of thiosulphate leaching of gold concentrate. The studied milled concentrate has shear-thinning fluid rheology and it was imitated by water-based solutions of CMC. Presence of electrolytes, as in the case of the leaching slurry, has great influence on bubble size distribution. Primary phase flow is measured by Particle Image Velocimetry. Local gas hold-up in aerated CMC 50000 (0.15 w%) solution is measured by Electrical Impedance Tomography. Volumetric mass transfer is measured by dynamic method in different CMC solutions over a range of operational conditions in absence and presence of electrolytes. The experimental data was used in CFD modelling of the aerated slurry. Single phase hydrodynamics of shear-thinning fluid (CMC 50000 (0.15 w%)) have been modelled and validated against experimental data with reasonable agreement. Multiphase mixing of the thiosulphate slurry was modelled with the assumption of constant bubble size. The results of the simulations and measurements are presented and discussed.

Keywords: Multiphase flow; Slurry mixing; PIV; EIT; CFD

Introduction

Thiosulphate leaching is a promising alternative to cyanidation, which is frequently used for selective dissolution of gold from ores and concentrates. Slow kinetics of thiosulphate leaching is often boosted by addition of copper (II). The copper oxidizes metallic gold transforming it to ionic form, which reacts with thiosulphate ligands producing stable gold-thiosulphate complexes. Ammoniacal media is required to prevent passivation by sulfur that might appear from the decomposition of thiosulphate when it reacts with ore [1]. It is suggested that ammonia transports gold ions to bulk solution by being more strongly adsorbed on gold surface [2]. Oxygen is needed to recover copper (II) from copper (I) at a little expense of slow thiosulphate oxidation by molecular oxygen [3]. Overall mechanism of gold leaching with thiosulphate can be briefly summarized by the following reaction [4]:

$$4Au + 8S_2O_3^{2-} + O_2 + 2H_2O \rightarrow 4Au(S_2O_3)_2^{3-} + 4OH^- \quad (1)$$

Selective dissolution of gold with the above-described reaction usually takes place in aerated stirred tanks. Continuous stirred-tank reactors (CSTR) of various types are frequently used in mining, chemical and biochemical industries to promote reaction by providing intensive mixing and high rate of mass transfer. In many cases, mixing affects conversion and yield of product. Poor mixing might result in stagnant zones. It is important to predict locations of stagnant zones. Providing good mixing benefits rate of mass transfer via effective renewal of fluids contact.

As computational power is constantly growing, numerical simulation of mixing tanks may efficiently reveal stagnant zones and help saving resources and time. In the last two decades, Computational Fluid Dynamics (CFD) has been successfully applied for modelling of multiphase hydrodynamics in stirred reactors of different types and shapes. Promising results in resolving flow fields as well as phase interaction parameters are well-described and analyzed in the review article of Joshi et al. [5]. Even though fluid dynamics modelling has been applied successfully to solve engineering tasks, CFD models of multiphase flows involve numerous empirical coefficients caused by spatial discretization and lack of knowledge about phenomena. This leads to uncertainties limiting application area. Tuning of empirical coefficients is a "compulsory measure" that requires validation procedure against experimental data.

There are many methods that have been designed to study fluid flow experimentally. Intrusive techniques such as Hot Wire Anemometry (HWA) are trustworthy and they can produce accurate results of high temporal and spatial resolution. However, they interfere flow and cannot measure many points synchronously [6]. Visual observations and measurements of hydrodynamics has taken significant place in hydrodynamics studies all along. Optical methods such as point-wise Laser Doppler Anemometry (LDA) and field-wise Particle Image Velocimetry (PIV) methods are extensively used in scientific studies dealing with optically transparent flows in stirred tanks [7-10]. For turbid and non-transparent flows Doppler Ultrasonic Velocimetry (DUV) has been developed. The operating principle of DUV is somewhat similar to PIV and it measures flow characteristics by means of ultrasonic beams reflected from seeding particles [11]. Measurements of Bubble Size Distribution (BSD) in mixed multiphase solution by tomographic PIV is challenging since images, taken in two-dimensional space and illuminated by laser pulse, give information on bubble size that is limited to particular area of laser sheet. In addition, local gas hold-up remains unknown in whole reactor. Application of Electrical Impedance Tomography (EIT), which is based on voltage measurements, has shown great potential in studies of multiphase flows for phase visualization in 3D [12-14]. Since conductivity is a function of gas hold-up, it is possible to obtain local void fraction of secondary phase by measuring voltages difference between primary phase alone and multiphase flow. Measuring voltage at several electrodes simultaneously

***Corresponding author:** Dmitry Vladimirovich Gradov, School of Engineering Science, Lappeenranta University of Technology, Lappeenranta, Finland, Tel: +358465470573; E-mail: dmitry.gradov@lut.fi

Received July 09, 2017; **Accepted** July 13, 2017; **Published** July 22, 2017

Citation: Gradov DV, González G, Vauhkonen M, Laari A, Koiranen T (2017) Experimental and Numerical Study of Multiphase Mixing Hydrodynamics in Batch Stirred Tank Applied to Ammoniacal Thiosulphate Leaching of Gold. J Chem Eng Process Technol 8: 348. doi: 10.4172/2157-7048.1000348

Copyright: © 2017 Gradov DV, et al. This is an open-access article distributed under the terms of the Creative Commons Attribution License, which permits unrestricted use, distribution, and reproduction in any medium, provided the original author and source are credited.

reconstruction of conductivity difference distribution and hence local gas hold-up is possible [15,16].

Studying of mixing hydrodynamics facilitates finding local k_L, which is needed to evaluate specific volumetric interfacial mass transfer rate in CSTR. Based on Higbie's penetration theory Kawase et al. [17,18] showed that mass transfer coefficient in liquid film for viscous fluids can be expressed through local energy dissipation:

$$k_L = C\sqrt{D_L}\left(\frac{\varepsilon\rho}{K}\right)^{\frac{1}{2(1+n)}}, \quad (2)$$

where ε is the turbulence energy dissipation rate, m^2/s^3, D_L is the gas diffusivity in liquid, m^2/s, ρ is the liquid density, kg/m^3, K is the consistency index, $Pa{\cdot}s^n$, n is the dimensionless flow behavior index, C is the proportionality coefficient. The effect of gas bubbles to the mass transfer coefficient is taken into account with the proportionality coefficient. The value of 0.301 for the coefficient, proposed by Kawase [18], has been tested by Garcia-Ochoa and Gomez [19] and was found to produce accurate results for gas-liquid mass transfer in stirred reactors.

In addition to local mass transfer coefficient, local interfacial area is also needed to evaluate local k_La. Measured locally distributions of bubble sizes and gas void fraction can provide information about local interfacial area between gas and liquid.

The idea of the current work is to acquire sufficient experimental data in order to be able to connect hydrodynamics of stirred multiphase flow to reaction kinetics. Thiosulphate leaching of gold in ammoniacal solution with the presence of copper (II) in stirred reactor was studied experimentally first and then simulated by means of CFD in order to get distribution of local mass transfer rate of oxygen into solution. The data presented in this study are useful for multiphase flows of finely-milled concentrate as well as for shear-thinning fluids agitated by Rushton turbine in aerated baffled reactors.

Materials and Methods

Object of study

The process of gold leaching with thiosulphate in ammoniacal solution, studied earlier [20] in a lab-scale batch STR, was taken as an example of typical multiphase pulp mixing process frequently encountered in mining and pharmaceuticals industries. The reaction proceeds under almost ambient conditions (atmospheric pressure and 30°C).

A lab-scale baffled stirred reactor, equipped with standard six-blade Rushton turbine, was investigated in the current research. A schematic representation of the vessel geometry and its dimensional parameters are presented in Figure 1. The impeller clearance was set at the distance equal to its diameter from the bottom of the tank. The gas sparger is a perforated metal pipe mounted at the bottom of the tank. The tank, made out of plexiglass, was designed and constructed in two versions. EIT uses controlled current injections to measure responding voltages at electrodes placed around the flow. Therefore, the vessel, meant to be used in EIT experiments, was equipped with electrodes on the walls arranged in rows. In particular, an arrangement of 4 rows consisting of 16 electrodes, made out of stainless steel, was mounted on perimeter of the reactor wall. Thus, approximate resolution of the spatial reconstruction is roughly 2 cm^3. Another tank of the same size was encased inside a rectangular plexiglass container to be filled with liquid of the same refractive index as the studied solution in order to eliminate visual distortions.

The power input per volume of fluid that was used in the reaction kinetics research was scaled via the known power number of the dual impeller to the reactor scale used in the current work. The scaled power input corresponds to the mixing rate of around 400 rpm.

Experimental techniques

Rheology study: The mean diameter of the gold concentrate particles used by Lampinen et al. [20] was 7 μm. [21] Having measured the total heat production in calorimeter (universal Calvet calorimeter C80 CS Evolution of SETARAM Instrumentation with reversing mechanism) as the function of solids content, and the maximum value corresponded to 30% of solids content, which was suggested to be optimal in the leaching solution. The range of the shear rate in the pulp mixing with the four different impeller speeds was roughly estimated using the PIV data (Figure 6) and the CFD model. Single phase mixing of the above-mentioned reactor was simulated in Fluent 16 and the results are summarized in Table 1. Looking ahead, rheological measurements of the gold concentrate suspended in water revealed shear-thinning behavior (Figure 4). The suspension used in the leaching experiments is non-transparent. Therefore, it is not suitable for hydrodynamics study by PIV. Suspended solids may also cause some bias when measured by

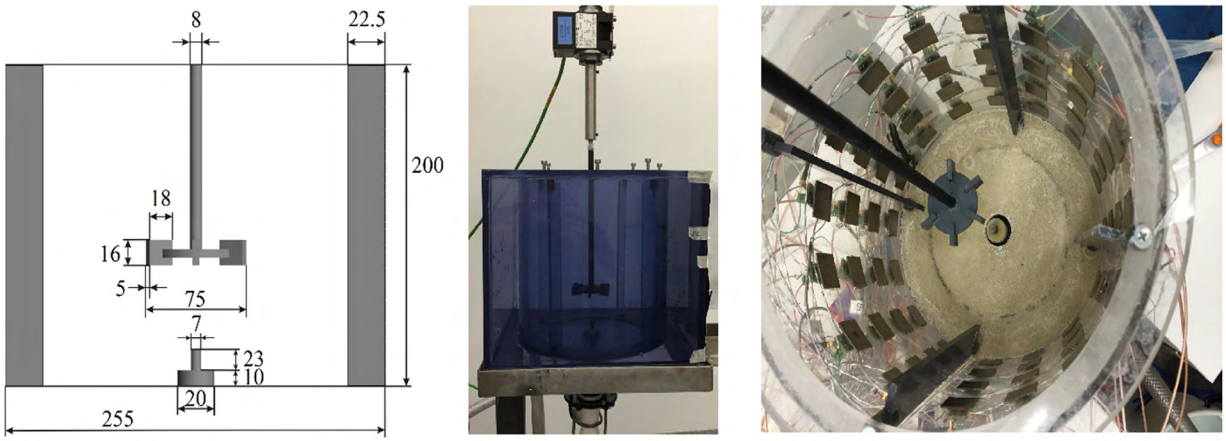

Figure 1: Reactor illustrations. a – scheme and sizing in mm, b – photo of the tank encased inside a plexiglass prism for PIV experiments, c – photo of the vessel equipped with electrodes for EIT experiments.

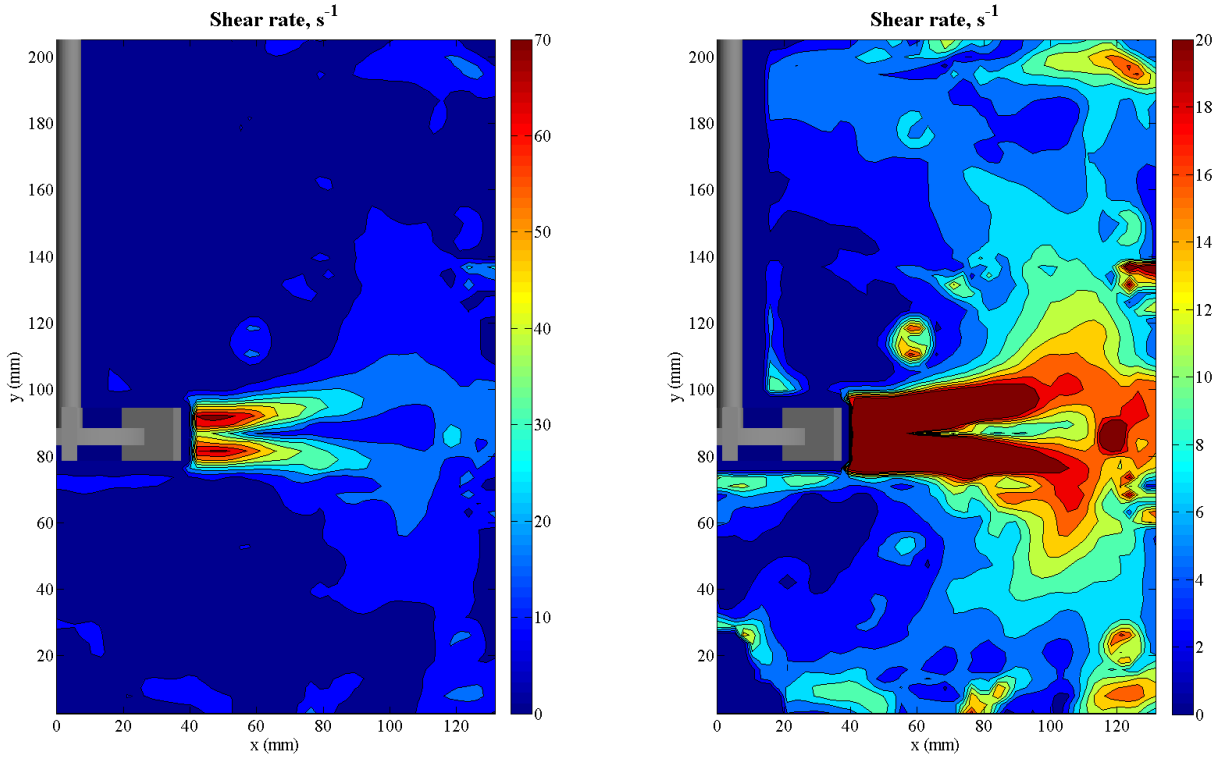

Figure 2: Contours of shear rate of CMC 50000 (0.15 w%) water-based solution at 400 rpm.

EIT due to conductivity difference between solids and liquid. For that reason, it was decided to imitate the solution experimentally by using Sodium Carboxy Methyl Cellulose (CMC) dissolved in water. Water solutions of CMC also have shear-thinning behavior and effect of CMC to rheological properties depends on molecular length. Two CMC powders were tested: CMC 30 and CMC 50000. The number going after CMC denotes viscosity of 2 % water-based solution measured at 25°C [22].

Dynamic Mechanical Analysis of the leaching pulp and water-based CMC solutions was performed using Anton Paar Modular Compact Rheometer 302. By means of swirling cone-analyzer (standard measuring cylinder CC27/T200/AL) the effective viscosity was measured in the shear rate range from 1 to 200 s^{-1}. Suspended solids in the leaching pulp had a tendency to sedimentate. Therefore, the pulp viscosity was measured additionally with a stirrer-sensor (ST24-2D/2V/2V-30/109). Measurements made by the cone and the blade analyzers produced similar results meaning that sedimentation for such tiny particles is a relatively slow process. Thus, the cone mixer-sensor was used alone in all the experiments in further.

Overall gas hold-up measurements: Gas hold-up measurements were made based on visual observation of liquid surface level of the agitated solutions. The reliability of the measurements was compromised by surface fluctuations and appearance of foam. In order to reduce uncertainties, the rise of the surface level Δh was measured at two positions: between the baffles next to the vessel wall. In each experiment, the agitated solution was allowed to reach equilibrium and then 10 readings from each point were made and averaged. The overall gas hold-up was computed based on the following equation:

$$\varepsilon_{\Delta h} = \frac{h_{gassed} - h_{ungassed}}{h_{gassed}}, \quad (3)$$

where $\varepsilon_{\Delta h}$ the overall gas hold-up, h_{gassed} and $h_{ungassed}$ are the heights of the mixed solutions with and without gas introduction correspondin gly.

EIT: The EIT set-up used in the experiments involved a signal generator, receiver, controller, and computer. The purpose of the signal generator is to produce current pulses of constant voltage to the solution according to a predefined scheme of pulses order. There are two different scenarios for the order of current injections that can be applied. Voltage injections can be sent pair-wise e.g., adjacent pairs of electrodes or multiple electrodes simultaneously. In both scenarios, voltages are measured at all electrodes. Then, obtained signal goes to demodulation process, where input voltage is decomposed into real and imaginary parts that are needed to get phase and amplitude according to the following formulations [23]:

$$v_{real} = \frac{2}{N}\sum_{i=0}^{N-1} v(\mathrm{i}) \sin\frac{2\pi i}{N} \quad (4)$$

$$v_{image} = \frac{2}{N}\sum_{i=0}^{N-1} v(i) \cos\frac{2\pi i}{N} \quad (5)$$

$$A = \frac{2}{N}\sqrt{v^2_{real} + v^2_{image}} \quad (6)$$

$$\varphi = \tan^{-1} v_{image} / v_{\mathrm{real}}, \quad (7)$$

where N is the number of electrodes, v(i) is the measured voltage

Impeller speed, rpm	γ s^{-1}			Method of determination
	Minimum	Maximum	Volume averaged	
100	0.002	350	2	CFD
200	0.005	708	5	CFD
400	0.012	1443	12	CFD
400	0	70	8	2D PIV plane (Figure 2)
600	0.024	2186	19	CFD

Table 1: Range of shear rate in the reactor.

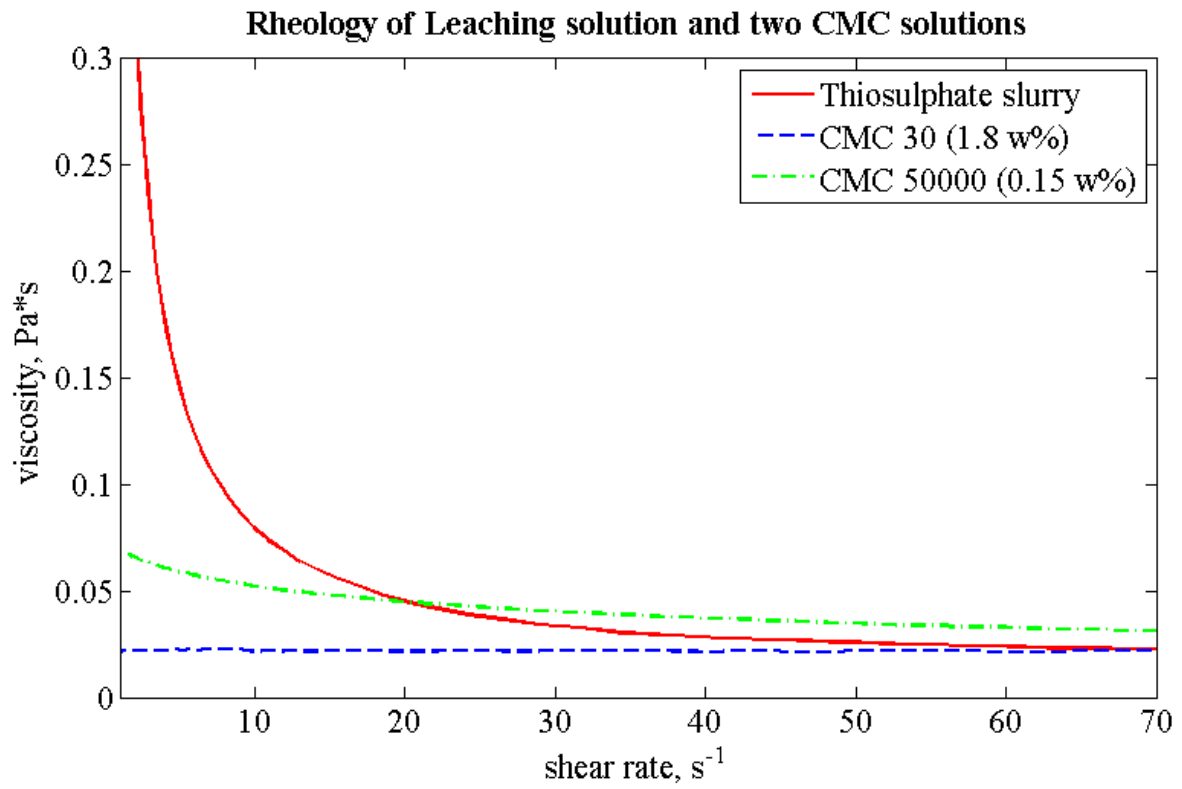

Figure 3: Rheological analysis of the leaching suspension and the two CMC water-based solutions of similar viscosity.

at i-th electrode, V, V_{real} is the real part of measured voltage, V, V_{image} is the imaginary part of measured voltage, V, ϕ and A are the signal phase and amplitude correspondingly.

Finding a conductivity distribution out of measured voltage outcomes of preset current injections represents itself an inverse problem. Computation of conductivity distribution is a challenging task to solve, since even a slight shift of voltages may be a result of significant change of conductivity distribution in solution, meaning that the "equation" might have several solutions. Therefore, some additional information about object of study is needed to solve the inverse problem. Prior information on conductivity distribution may be achieved statistically and used as a reference [23,24].

The difference method exploits measurements of non-gassed mixed solution as a reference in order to get gas void fraction distribution in the reactor. The conductivity distribution is the function of fluid resistance, and hence, local gas hold-up could be found as follows [23]:

$$\varepsilon_{EIT} = \frac{2(\sigma 1 - \sigma 2)}{2\sigma 1 + \sigma 2}, \quad (8)$$

where σ_1 is the conductivity distribution of liquid phase, S/m, σ_2 is the conductivity distribution of dispersed gas phase, S/m. Thereby, the difference method automatically removes the influence of non-conductive parts of the vessel such as baffles and impeller.

Many researches describe successful applications of the technique for stirred tanks to measure local gas hold-up [13,14,25-28]. Value of current injections value is dictated by conductivity of the studied solution. The higher the solution conductivity, the higher the current injections are required in order to increase sensitivity of the system.

PIV: Particle Image Velocimetry was used to study the hydrodynamics of the liquid phase agitated in multiphase mixing. The PIV technique measures velocity flow fields by capturing the movement of tracing particles, which are small enough not to interfere the flow. By slicing the flow with a laser sheet, PIV can produce a two-dimensional picture of the fluid motion within the laser sheet of illumination. A vector velocity field is constructed based on spatial shift of tracer-particles between a pair of laser pulses emitted consecutively in accordance with a preset time delay. The PIV set-up included a double-pulsed Nd:Yag laser and two Charge-Coupled Device (CCD) cameras of the following resolution 1600 × 1200 pixels. The laser and the cameras were managed by Davis 7.2 PIV software. The imaging of tracers shift was carried out by two CCD cameras which were

synchronized with laser pulsing. Thus, velocity vector fields of axial and radial components were measured in 2D space.

In order to measure liquid phase flow, fluorescent particles of size 20 – 50 µm, made of polyamide, were used as tracers. The fluorescent tracers emit light at different wavelength than the laser. This property facilitates getting images with uniformly illuminated background. High bandpass filters (Light red bandpass filter: BP635) were installed on the CCD cameras to separate light within the wavelength range 615 – 645 nm to filter out the green light coming from light-reflecting surfaces of the reactor [29]. Gas bubbles pictures were made using the light reflected from bubbles. In this case, a camera was capped with a grey filter (B+W, 52 103 ND 0.9 8x) only to reduce intensity of the reflected light.

The laser sheet in the reactor was positioned vertically near the baffle and 2 mm behind the vertical axe of the shaft. The reason for this positioning was to remove as many visual obstacles and strong reflections as possible. Size of single frame taken (measurement window) depends on camera resolution and focal length of objective. A typical size of the measurement frame was 127 × 100 mm. Such frames were processed twice via cross-correlation algorithm. At first, the frame square is split by the PIV software into interrogation areas of 128 × 128 pixels to search vectors. Then, interrogation areas were decreased to 64 × 64 pixels with 50% overlap and the frame was treated in similar way to search for tracers shift with higher precision. The final PIV results have resolution of 2.2 mm. A sample of the taken frames and the resulting vector field of instantaneous and average velocities are presented in Figure 3. In order to get a full picture of the reactor, it was necessary to take three frames at different heights along the vertical axe with 50 mm overlapping (Figure 5). Thus, when the captured frames were assembled, a full image of the reactor, from the tank wall to the shaft, of size 127 × 200 mm could be obtained. The resolution of post-processed and vertically combined frames was 51 × 79 vectors. Totally 1000 frames were taken and processed in order to obtain time-averaged results.

k_La measurements: Volumetric mass transfer coefficient was measured via "gassing-out" dynamic method by using dissolved oxygen meter MARVET BASIC. All the experiments were performed at 20°C. The reactor was at first bubbled with nitrogen until dissolved oxygen concentration reached its minimum. Then a valve of nitrogen pipe line was closed and air was introduced. The evolution of the changing oxygen concentration was recorded until it reached its maximum value. The data was analyzed by parameter estimation software MODEST [30] and the volumetric mass transfer rate was calculated using using Eq. 9.

$$\frac{c_{sat}-c_{liquid}(t_1)}{c_{sat}-c_{liquid}(t_2)}=\frac{e^{(-k_La\,t)}-k_La\tau_p e^{-t/\tau_p}}{1-k_La\tau_p}, \quad (9)$$

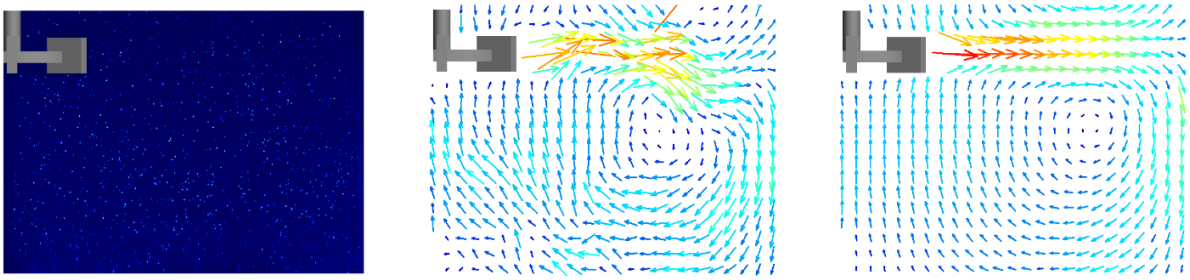

Figure 4: Measurement window and the calculated velocity vector fields near the impeller. a – PIV frame, b – instant velocity vector field, c – averaged velocity vector field.

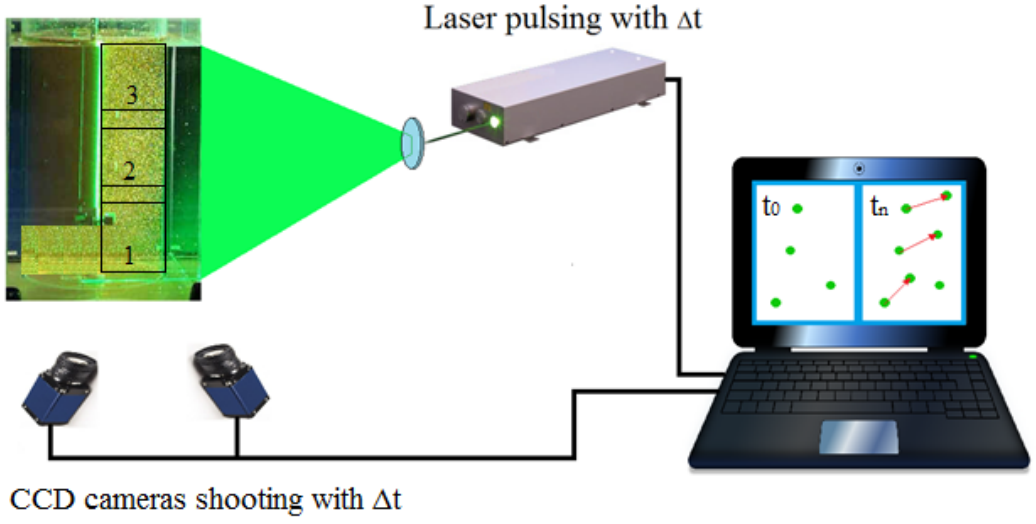

Figure 5: Schematic representation of PIV set-up

where c_{sat} is the saturated oxygen concentration in water, mol/m^3, c_{liquid} is the oxygen concentration in liquid, mol/m^3, at t_1 and t_2.

Time constant shows how quickly a measuring probes responses to a sudden step change of oxygen concentration. In order to expect accurate results the value of the time constant should be lower than k_La^{-1} [31,32]. The response time constant τ of the probe was measured separately for each solution studied. In the experiments, the oxygen probe was placed between baffles where the mixing is vigorous and the bulk solution around the probe is constantly renewed by the flow. Otherwise, the probe might consume all the oxygen presented in the bulk around at some moment and further measurements become inaccurate.

Modelling theory

Multiphase fluid flow: The Stoke's number (Eq. 10) for the studied system is more than 1, meaning that the secondary phase influence onto the primary phase is not negligible and it has to be taken into account.

$$St = \frac{\tau_p}{\tau_q} = \frac{d^2{}_p \varepsilon^{0.5}}{36\nu^{1.5}}, \quad (10)$$

Where τ_p and τ_q are the relaxation time of primary phase and bubble, s, d_p is the bubble diameter, m, ε is the energy dissipation, m^2/s^3, ν is the kinematic viscosity, m^2/s.

Therefore, in the gas-liquid modelling, Eulerian-Eulerian multiphase approach was used, in which gas and liquid phases are considered as interpenetrating continua. A set of conservation equation is solved for each phase (Eq. 12 and 13). Additionally, volume fraction is introduced (Eq. 11).

$$\sum_i a_i = 1 \quad (11)$$

$$\nabla \overline{u} = 0 \quad (12)$$

$$\overline{u}.\nabla\overline{u} = -\nabla\overline{p} + \nabla.[(\mu + \mu_{turb})\nabla\overline{u}], \quad (13)$$

where α_i is the phase volume fraction, $\overline{u}$ - phase velocity, m/s, $\overline{p}$ is the pressure, Pa, μ_{turb} is the turbulent viscosity, Pa·s.

Suspended solids: The tiny milled concentrate was used in the original leaching tests with mean size of 7 μm. Pulp flow can be modeled via effective viscosity [33]. Rheology of the leaching slurry has been measured experimentally and modelled via power-law model (Eq. 23).

Turbulence: In CFD modelling, available computing power and acceptable simulation time were limited, for which reason it was decided to apply a Reynolds-Averaged Navier-Stokes (RANS) turbulence model in the current simulations. Turbulence formulation in RANS models are based on statistical analysis rather than on actual physical phenomena. By contrast, the Large Eddy Simulation (LES) model is based, at least partially, on resolving turbulence fluctuations. Approximations such as the Boussinesq hypothesis can lead to mismatches with real flow behavior due to turbulence isotropy and homogeneity. As a result, empirical constants are introduced to tune the model (Eq. 14 and 15). In the current work, it was decided to evaluate the suitability of the most frequently applied RANS models rather than attempt to implement a novel turbulence model by tuning the model constants for the hydrodynamics of the specific stirred tank. In our previous work [34], three popular models in the RANS family were tested, namely the Realizable k-ε model, the Shear Stress Transport k-ω model, and the Reynolds Stress Model (RSM). The Realizable k-ε model produce the most accurate results for single and multiphase mixing in round bottom STR. The Realizable k-ε model is a recent model with an improved computational mechanism preventing turbulence energy from being negative. Such energy is not physical but can occur using the Standard k-ε model.

$$\overline{u}\cdot\nabla k = P - \varepsilon + \nabla\cdot\left[\left(\mu + \frac{\mu_{turb}}{\sigma_k}\right)\nabla k\right] \quad (14)$$

$$\overline{u}\cdot\nabla\varepsilon = C_{\varepsilon 1}\frac{\varepsilon}{k}P - C_{\varepsilon 2}\frac{\varepsilon^2}{k}P + \nabla\cdot\left[\left(\mu + \frac{\mu_{turb}}{\sigma\varepsilon}\right)\nabla\varepsilon\right], \quad (15)$$

where k is the turbulence kinetic energy, m^2/s^2. Production P includes one more constant.

Dispersed turbulence formulation model was used since the secondary phase is dilute and fluctuating quantities of the gaseous phase may be found as the function of the mean terms of the liquid phase. At first, turbulence terms k and ε are first computed for primary phase. Then, secondary phase turbulence terms are found and exchange of turbulence momentum between phases is computed based on Tchen-theory [35].

Phase interaction: Momentum conservation equation (Eq. 16) includes cumulative force $\vec{F}_q$ (Eq. 17) acting on primary phase. The cumulative force comprises several forces occurring in multiphase interaction, including drag, virtual mass, lift, wall lubrication, turbulence diffusion forces etc.

$$\frac{\partial}{\partial t}(\mathrm{ap}\vec{\mathrm{u}})_q + \nabla\cdot(\mathrm{ap}\vec{\mathrm{u}}\vec{\mathrm{u}})_q = \nabla\cdot(\mathrm{a}\sigma)_q - \mathrm{a}_q\nabla p + \vec{F}_q + a_q p_q \vec{g} \quad (16)$$

$$\vec{F}_q = \sum_{p=1}^{n}(\mathrm{k}_{pq}(\vec{\mathrm{u}}_p - \vec{\mathrm{u}}_q) + \dot{\mathrm{m}}_{pq}\vec{\mathrm{u}}_{qp} - \dot{m}_{qp}\vec{\mathrm{u}}_{qp}) + (\vec{F}_q + \vec{F}_{lift,q} + \vec{F}_{wl,q} + \vec{F}_{vm,q} + \vec{F}_{td,q}), \quad (17)$$

where $\vec{F}_q$ is the external body force, $\vec{F}_{wl,q}$ the lift force, $\vec{F}_{wl,q}$ is the wall lubrication force $\vec{F}_{vm,q}$ is the virtual mass force, and $\vec{F}_{td,q}$ is the turbulence diffusion force.

Different drag models can be found in published literature. The most popular model, proposed by Schiller and Naumann [36] in Eq. 19, is a drag model suitable for rigid spherical particles.

$$kpq = \frac{\rho_p C_D \mathrm{Re}}{144\tau_p}\mathrm{d_p A_i}, \quad (18)$$

where ρ_p is the particle density, kg/m^3 C_D is the drag coefficient, A_i is the relative Reynolds number, and A_i is the interfacial area, m^2. The drag force coefficient is the function of Re according to the following formulation:

$$CD = \begin{cases} 24(1 + 0.15\,\mathrm{Re}^{0.687}) & \mathrm{Re} \le 1000 \\ 0.44 & \mathrm{Re} > 1000 \end{cases} \quad (19)$$

The drag force model is based on bubble rise velocity measured in stagnant fluids, which is higher than rise velocity in turbulent flow. A model correcting drag force coefficient for turbulence was proposed by Brucato et al. [37]. This turbulence modification factor concept (Eq. 20) changes stagnant fluid drag force to make it suitable for adoption in turbulent multiphase flow simulation Later, Lane et al. [24] critically considered Brucato's formulation and found that ratio of slip and terminal velocity as a function of bubble size and Kolmogorov length scale does not take into account particle density or density difference between phases. Having pointed out this deficiency in Brucato's model, Lane et al. suggested a new correlation (Eq. 21) for turbulence modification factor that is based on ratio of stagnant to turbulent terminal velocity $\frac{U_s}{U_T}$ to be correlated with ratio of particle relaxation time to integral time scale of turbulence (Eq. 22).

$$K'_{pq} = \eta K_{pq} = \left(1 + K\left(\frac{d_p}{\lambda}\right)^3\right)K_{pq}, \quad (20)$$

Where η is the turbulence modification factor, K= 6.5·10-6, λ is the Kolmogorov length scale, m.

$$\eta = \left(1 - 1.4\left(\frac{\tau_p}{T_L}\right)^{0.7} e^{\left(\frac{0.6\tau_p}{T_L}\right)}\right)^{-2} \quad (21)$$

$$T_L = 0.135\frac{k}{\varepsilon}, \quad (22)$$

Gradov et al. showed that the Schiller-Naumann drag force model in conjunction with Lane's turbulence modification factor gave the most accurate results for air-water mixing in stirred tank at the assumption of constant bubble diameter equal 1 mm. Also, the effect of non-drag forces was found to be insignificant air-water mixing simulations. Therefore, in order to reduce computational complexity and promote solution stability the above mentioned combination of models was used to simulate drag force, while other forces models were ignored [34].

Modelling strategy: In the gas-liquid flow simulations, the gas was introduced into converged liquid flow field in order to reduce computational instabilities. In the CFD simulations, the stirred tank can be considered as a semi-batch system with gas is supplied via sparger and exit through liquid surface. The gas phase was introduced in a transient manner at 0.02 s time step until mass flow rate balance was reached and stabilize within 5% deviation. Under relaxation factors for pressure and velocity were reduced up to 0.15 and 0.35 correspondingly to facilitate convergence. Second order discretization scheme was applied to all the parameters. Convergence criterion was set at 10^{-4} for all the variables to be simulated. When multiphase flow hydrodynamics have been computed, mass transfer was calculated on top of multiphase results according to Eq. 2. The operational conditions simulated and models used in single phase and multiphase mixing simulations are summarized in Tables 2 and 3.

Results and Discussion

Experimental results

Rheology: The rheology of the leaching suspension as well as the water solutions of CMC 50000 (0.15 w%) and CMC 30 (1.8 w%) were measured and shown in Figure 3. The presented data was plotted in log-log scale, and the rheological parameters were found from the Ostwald-de Waele power law [38]:

$$\mu_{eff} = K\left(\dot{\gamma}\right)^n, \quad (23)$$

where μ_{eff} is the effective viscosity, Pa·s, K is the consistency index, Pa·s^n, n is the flow behavior index.

The viscosity of all the solutions approach constant level as the shear rate is increased. However, only the solution of short molecular chain CMC 30 shows insignificant shear-thinning rheology. Therefore, only CMC 50000 has been used in further as an imitation model of leaching suspension. It is advisable to set limits for the effective viscosity when modelling non-Newtonian hydrodynamics in order to avoid numerical errors. Calculated power law parameters are summarized in Table 4.

Gas hold-up: Measurement of gas hold-up in STR by level difference has better accuracy at high gas hold-ups. Gas hold-up has linear dependence on superficial velocity as described by Rewatkar et al. [39] numerically and approved experimentally experimentally later by Kraume and Zehner [40] for glass beds suspended in water and by Laakkonen [41] for Xanthan solutions. In the current study, gas hold-up was measured over the range of gas flow rates from 1 to 10 L/min at constant impeller speed of 400 rpm. The results are plotted in Figure 6.

The obtained results show almost linear dependence of gas hold-up from gas flow rate. It is necessary to use relatively low gas flow rate in PIV measurements to ensure good optical transparency of solution and reduce impact of gas bubbles onto laser intensity. Therefore, gas flow rate could be safely reduced to 1.25 L/min.

EIT: Increased viscosity promotes growth of bubble size due to increased coalescence rate. However, it is also known that presence of electrolytes in solution inhibits bubble coalescence [42]. At sufficiently high salt concentrations, bubbles, covered by ion layer, repel each other. The total optimal concentration of salts for thiosulphate leaching was found to be 0.4 mol/L [20]. Unfortunately, the EIT set-up loses its sensitivity at high conductivity of solution since the maximum current was limited to 6.5 mA. For that reason, the salt concentration had to be reduced to lower value, where a compromise between the similarity in the multiphase solution properties compared to the original solution and the set-up limits could be met. It can be concluded, that significant amount of ions in liquid suppresses the bubble-growing effect generated by higher viscosity. The influence of the salt concentration on gas phase can also be tested indirectly by measuring the power draw of the impeller. Impeller torque was measured as salts were added step-wise (0.05 mol/L per step). The results (Figure 7) show that 0.05 mol/L of salts was enough to effectively cover the major part of the bubbles surface in the solution. Further addition of salts has insignificant effect on the mixing power and hence on the gas hold-up. However, the power draw is manly driven by the average density of the multiphase solution, and it is little influenced by the distribution of bubble size which has, however, significant influence on the contact surface area between the phases. Therefore, the overall k_La was also measured at different salt concentrations, as depicted in Figure 9 (left plot) as depicted in Figure 7 (left plot) (left plot). The slow increase of the overall mass transfer is an evidence of the ongoing shift in the BSD towards small bubbles. At concentration 0.1 mol/L, with a conductivity of 7.9 mS/m (which is within the maximum conductivity limit of the EIT), the k_La value is 91% of the maximum k_La value at concentration 0.4 mol/L. Therefore, this concentration was selected as a reasonable compromise and was used in all the experiments.

In order to evaluate the performance of the EIT set-up, several experiments were made at three gas flow rates without mixing. The

Operational conditions	Modelled phenomenon	Model used
400 rpm	Turbulence	k-ε Realizable
	Shear-thinning rheology of mixed fluid	Power-law model
	Flow near the solid walls	Standard wall function

Table 2: Summarized conditions for single phase mixing simulations.

Operational conditions	Modelled phenomenon	Model used
400 rpm	Turbulence	k-ε Realizable
	Shear-thinning rheology of mixed fluid	Power-law model
1.25 L/min of air flow rate	Flow near the solid walls	Standard wall function
	Bubble size	Constant d_b=1.5 mm

Table 3: Summarized conditions for multiphase mixing simulations.

Solution	n	K, Pa·s^n	μ_{min}, Pa·s	μ_{max}, Pa·s
Thiosulphate slurry	0.200	0.044	0.02	0.40
CMC 50000 (0.15 w%)	0.746	0.086	0.02	0.09

Table 4: Power law model parameters.

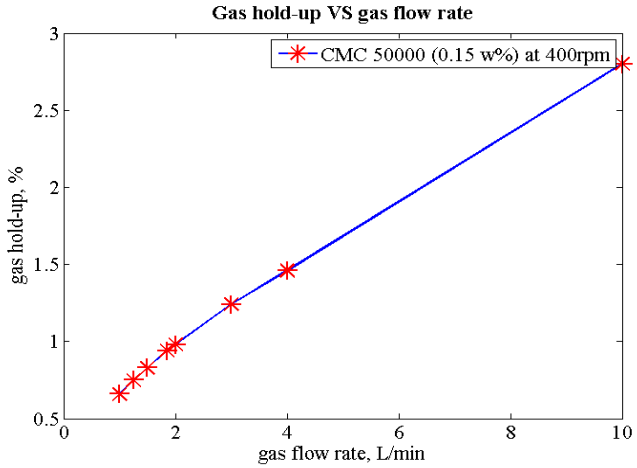

Figure 6: Gas hold-up vs superficial gas velocity in CMC 50000 (0.15 %) water-based solution at 400 rpm.

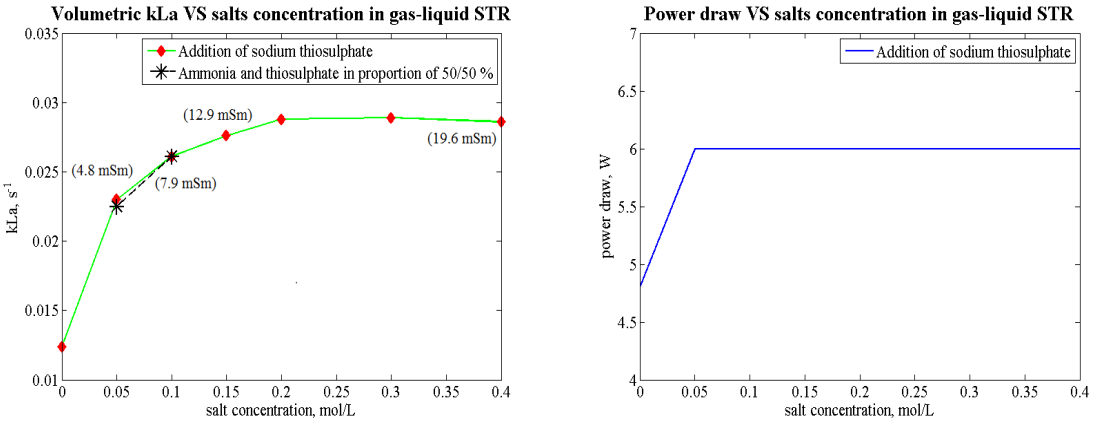

Figure 7: Overall kLa (right) and power draw (left) with conductivity of CMC 50000 (0.15 %) water-based solution at 600 rpm and 2 L/min gas flowrate vs salt concentration

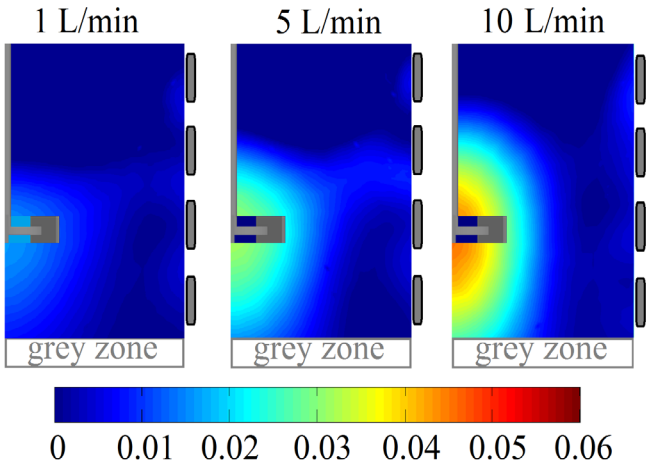

Figure 8: Local gas hold-up in CMC 50000 (0.15 %) and 0.1 mol/L of sodium thiosulphate in 2D plane (middle plane positioned between the baffles) measured by EIT without mixing.

obtained local gas hold-ups are illustrated in Figure 10. The resolution of the resulting images was around 2 cm^3. It is clear that at large flow rates, the contrast in gas-liquid conductivity is high and the EIT results of gas-liquid mixing become more reliable.

The local gas hold-ups of the water-based solution of CMC 50000 mixed at 200, 400 and 600 rpm over the range of gas flow rates from 1 to 2 L/min are presented in Figures 10-11.

The overall gas hold-ups increase as the gas flow rate is increased with all the impeller speeds tested. Unfortunately, the poor resolution of the EIT set-up does not capture small bubbles present in high quantities in the most agitated region around the impeller. At low gas flow rates and high impeller speeds conditions are challenging when bubbles are smaller and distributed more uniformly in the volume of the reactor. Decreased and evenly distributed gas void fraction allows electrical current bypassing small bubbles especially at high loads of electrolytes in the solution. The measured zero value of gas hold-up around the impeller indicates narrow size distribution of small bubbles. The bubbles become traceable only in the region of low turbulence intensity where bubble coalescence takes place. The regions of bubble growth are most distinct at low ratio of impeller speed to gas superficial velocity. It can be noticed that bubble size grows in radial direction towards the wall. Below the impeller, a down pumping circulation loop generates a stagnant zone where the retention time of bubbles is bigger. Meanwhile, bubbles, escaping the loop, gravitate to the free surface and move into less turbulent region where they coalesce. In addition, intensive foaming takes place when the CMC-water-thiosulphate solution is mixed which facilitates accumulation and growth of bubbles near the free surface. As a result, high local gas hold-up next to the surface is formed which is also presented in all the figures.

PIV: PIV results of CMC 50000 (0.15 w%), showing contours of the averaged velocity vector field and the r.m.s instantaneous velocity field, are shown in Figure 12. The averaged velocity vector field is a great source of information. The spatial velocity gradients may give information about the range of shear rate in the 2D slice of the flow (Figure 2). That information was used to define the range of shear rate in the rheology study of the suspension and the CMC water-based solutions. When studying the shear rate distribution in the PIV plane more closely one may notice that the agitated flow is rapidly attenuated in the viscous solution. It can be clearly seen that the visible stable streams which have shear rates of 70 s^{-1} are pushed by the agitator and dissipated into the bulk solution where the initial shear rate is reduced

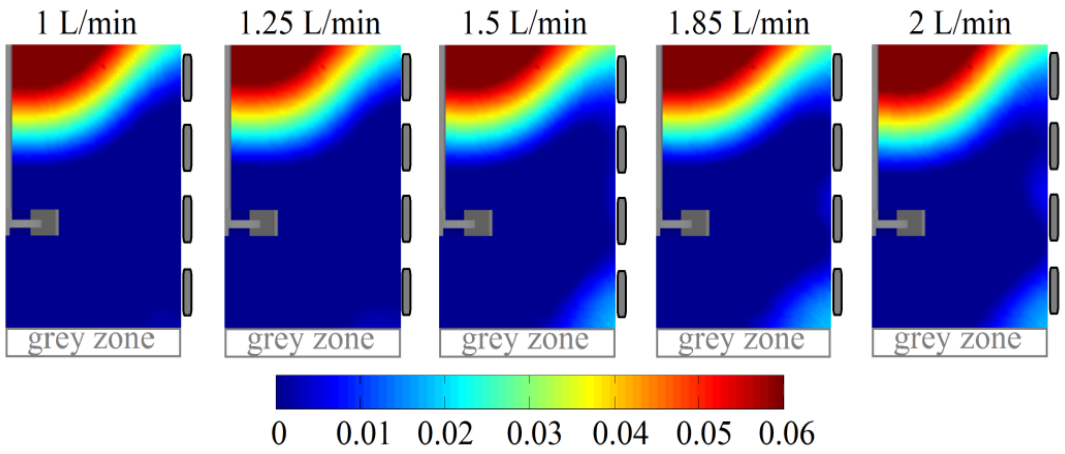

Figure 9: Local gas hold-up in water solution of CMC 50000 (0.15 %) and 0.1 mol/L of sodium thiosulphate in 2D plane (middle plane positioned between baffles) measured by EIT at 600 rpm and the range of gas flow rate.

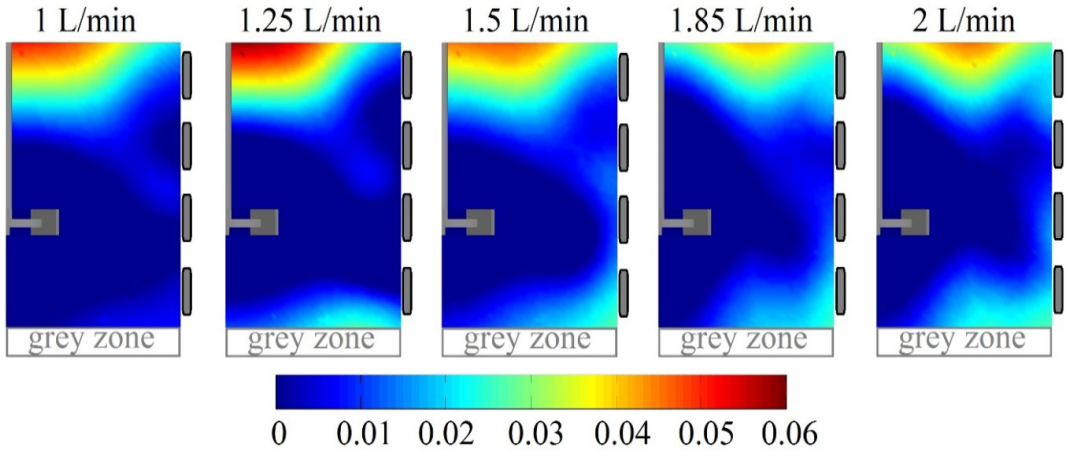

Figure 10: Local gas hold-up in water solution of CMC 50000 (0.15 %) and 0.1 mol/L of sodium thiosulphate) in 2D plane (middle plane positioned between the baffles) measured by EIT at 200 rpm and the range of gas flow rate.

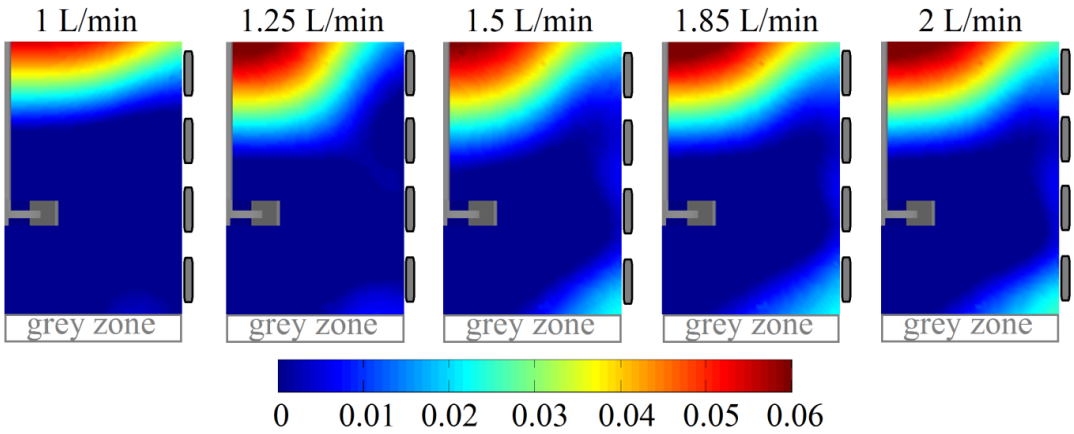

Figure 11: Local gas hold-up in water solution of CMC 50000 (0.15 %) and 0.1 mol/L of sodium thiosulphate in 2D plane (middle plane positioned between baffles) measured by EIT at 400 rpm and the range of gas flow rate.

to around 10 s^{-1}.

Salts free single phase mixing of the CMC solution at 400 rpm (Figures 2 and 6) at 1.25 L/min were measured by the PIV and used for validation of CFD results.

As it was stated earlier, the leaching solution used in the original tests of thiosulphate leaching of gold [20] had high salts concentration. In the PIV tests, CMC 50000 (0.15 w%) solution with 0.1 mol/L concentration of sodium thiosulphate was used to study gas bubbles. Presence of salts has significant impact onto BSD. Ions of the same sign cover surface of gas bubbles and block coalescence rate by repelling mechanism. As a result, one may notice narrow distribution of gas bubbles in Figure 13.

Bubble size distribution is almost uniform in the most turbulent region next to the impeller as well as also elsewhere in the image. Bubble size varies from 1 mm to 1.8 mm as it is seen in the zoomed picture. The bubbles are densely populated in the plane of measurement. However, it should be mentioned that only those bubbles that are in focus were considered when evaluating the bubble size.

Such a narrow range of BSD may be approximated as a constant bubble size (1.5 mm) throughout the reactor under the current conditions. Considering CFD modelling this approximation greatly simplifies modelling and use of Population Balance Model (PBM) can be avoided.

Overall k_La: Two water-based solutions of CMC 30 (1.8%) and CMC 50000 (0.15%) were used to measure the volumetric mass transfer coefficient at three impeller speeds and the range of gas flow-rates with and without addition of salts. The results are presented in Figure 14.

The volumetric mass transfer rate is proportional to interfacial contact area and mixing intensity. At mixing speed 600 rpm k_La grows as gas flow rate is increased. However, at lower mixing speeds k_La increases up to some point and then goes down with the increase of gas input. The reason for this behavior is the contact area that drops if mixing intensity is not enough to keep the bubble size small. Without salts both CMC solutions have similar mass transfer due to similar apparent viscosity. Presence of ions in water-based solution of CMC 30 does not lead to significant drop of viscosity and the similar mass transfer can be observed. However, ion presence affects CMC 50000 so that the long chain molecules are broken and the apparent viscosity of solution is decreased. Low viscosity and high content of ions in the solution give nearly constant and small bubble size that results in high values for k_La.

Numerical results

Grid independence test: Spatial discretization influences results of numerical simulation. Five different grids have been tested. Water mixing simulations were used in grid independence study. Reactor geometry was meshed with almost doubling factor relatively one another and scaling uniformity was maintained as well. Re number differs significantly within the vessel therefore 14 sampling points of velocity have been defined in the reactor domain. A normalized root mean square error index (NRMSE) was employed as a criterion for grid independency validation [43]. Its formulation is as follows:

$$\mathrm{NRMSE} = \frac{3}{\left(\frac{N_{fine}}{N_{coarse}}\right)^{p^*} - 1} \sqrt{\frac{\sum_{i=1}^{n}\left(\varphi_1(i) - \varphi_2(i)\right)^2}{\sum_{i=1}^{n}\left(\varphi_2\right)^2}} \cdot 100\% \qquad (24)$$

where N is number of cells in a grid (it is advised to keep grid size ratio above 1.3 corresponds to order of discretization, n is number of samples, φ_1 and φ_2 are predictions on coarse and fine grids accordingly.

According to the authors, grid difference might be considered negligible if NRMSE value is less than 10%. During mesh sizing independence tests simulations were performed with second order discretization scheme. Results presented in Table 5 clearly indicate grid 4 to be optimal one for the needs of the current study.

Shear-thinning fluid mixing: To reduce numerical instability the gas-liquid multiphase simulation strategy included two steps. The gas-liquid simulations were made in two-way coupling. At first,

Grid name	Number of elements	Torque, mNm	∫kdv $m^2/s^2 \cdot 10^{-5}$	∫εdV, $m^2/s^3 \cdot 10^{-5}$	NRMSE $\bar{u}$ %
1	108 276	54.0	9.9	139.2	20
2	269 654	56.0	10.8	161.2	13
3	464 532	56.6	10.7	166.4	15
4	754 056	65.6	13.0	209.1	9
5	1 969 376	64.4	12.6	208.5	NaN
Measured experimentally		**65 ± 3**			

Table 5: Grid test results of water mixing at 400 rpm in STR.

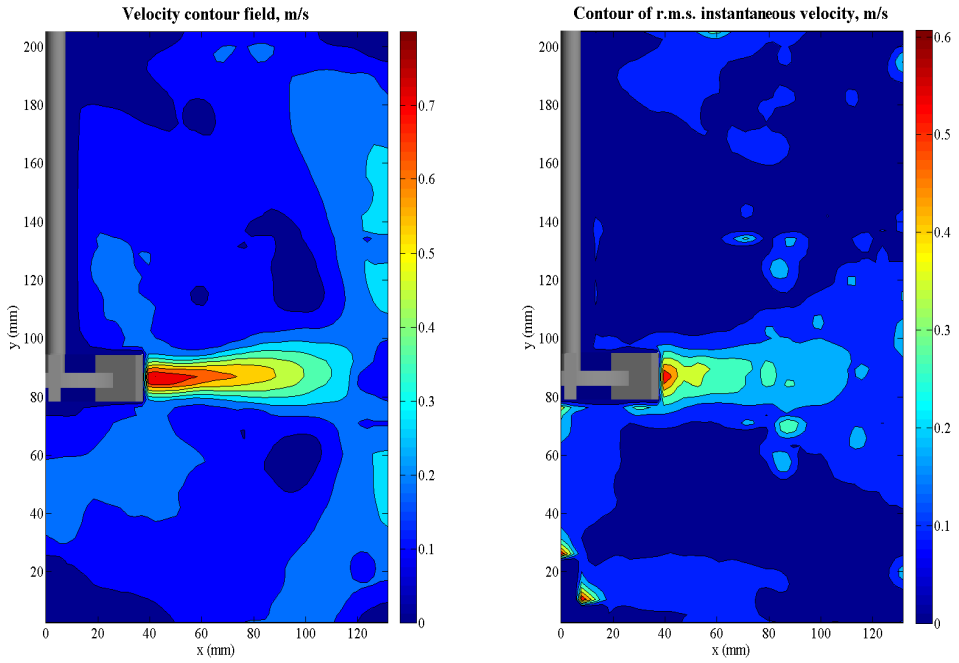

Figure 12: Velocity field contour (left) and contour of r.m.s. instantaneous velocity (right) for CMC 50000 (0.15 w%) water-based solution at 400 rpm.

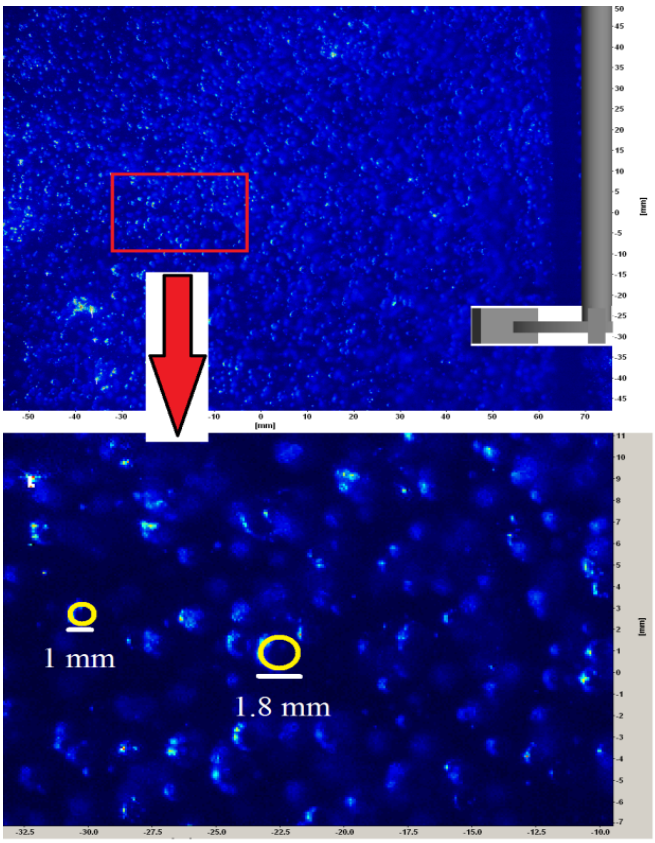

Figure 13: PIV frame with measured bubble sizes in CMC 50000 (0.15 %) water-based solution with salt addition (1 mol/L) at 400 rpm and 1.25 L/min gas flow rate.

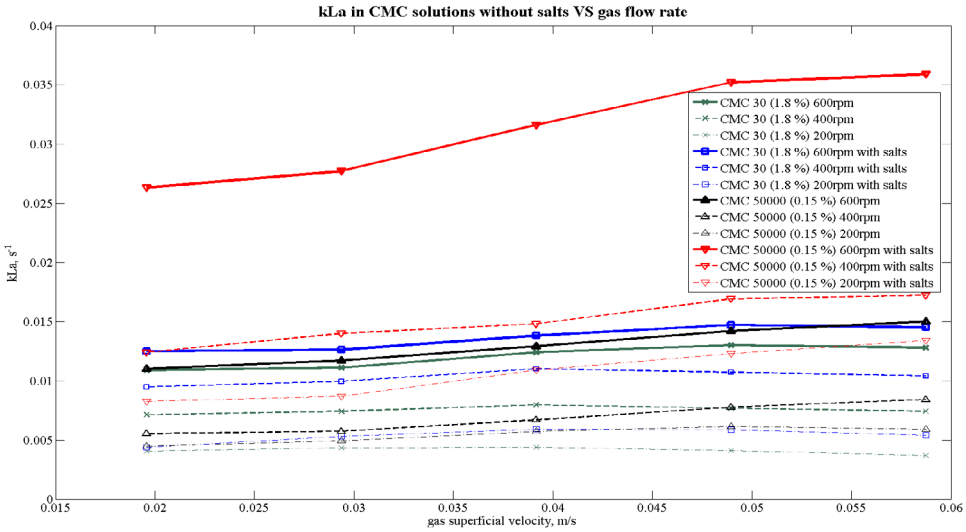

Figure 14: Measured overall kLa via dynamic method for water-based solutions of CMC 50000 (0.15 %) and CMC 30 (1.8 w%) in gas-liquid STR alone and in presence of salts (1 mol/L).

primary phase flow has been resolved, converged solution results of which were used as initial data before activation of secondary phase. It is important to resolve primary phase accurately because primary phase hydrodynamics has great impact onto secondary phase. Before gas phase introduction in a transient manner, the simulation results of mixed non-Newtonian solution were validated against experimental results.

Qualitative analysis was performed by comparison of the velocity contour fields in vertical 2D plane sampled at the identical spatial position and it is shown in Figure 15. Particle Image Velocimetry used in this work measured only two velocity components out of three. Therefore, the velocity contour of CFD simulation results was adjusted for qualitative comparison and includes only radial and axial components. The tip speed of the Rushton turbine rotating at 400 rpm is 1.57 m/s. Radial and tangential at the tip of impeller can be equaled. However, accurate measurements of impeller jet-stream are complicated by rotating blades of the turbine and slight swinging of the shaft. That makes slight underprediction of maximum radial velocity component in the impeller region in PIV measurements.

Overall velocity distribution profiles look quite similar between CFD and PIV results. Both circulations taking place above and below jet-stream are captured at the same locations and in similar manner. However, jet-stream velocity field profile is a bit thicker in CFD contour. It could be explained by isotropic turbulence being used by the turbulence model, while the flow turbulence produced by a Rushton turbine is anisotropic [44,45].

Since velocity filed contours comparison might be biased, the velocity components normalized with the tip speed were validated against experimental results in radial profiles (Figure 16). In order to sample hydrodynamics at different regions of the reactor, the profiles were taken at three vertical positions 30, 80 and 150 mm starting from the bottom. The simulation of shear-thinning flow agitated by the Rushton turbine describes the flow accurately.

Power draw was found experimentally by measuring torque via on-shaft torque transducer. The measured and simulated torque of single phase mixing of CMC 50000 (0.15 w%) and the leaching slurry are presented in Table 6. As expected, the reduction of power draw is observed in case of gas-liquid mixing, because average density of multiphase solution is lower than of single phase. The torque of mixed CMC 50000 was simulated accurately.

Aerated slurry mixing: When the solution of the leaching slurry mixing has reached convergence, air has been introduced via velocity inlet in transient manner with 0.02 s as time step. The simulation lasted until the balance of air mass flow rate was observed. Average density of the suspension (30 w%) is 1570 kg/m^3.

Average velocity field of the mixed slurry is presented in Figure 17. Maximum value of velocity magnitude is around tip speed. One may notice velocity contour of the air jet supplied via sparger.

As it was found during the gas bubbles study in PIV section, the BSD is very narrow in presence of electrolytes (0.1 mol/L). Therefore, 1.5 mm bubble size was used in the simulations. Specific volumetric surface area of secondary phase can be found as follows:

$$A_p = \frac{6\varepsilon_p}{d_p} \quad (25)$$

where ε_p is the volume fraction of secondary phase, fraction.

The volume fraction and specific surface area of gas phase in the mixed slurry are shown in Figure 18. On one hand, high apparent viscosity of the leaching slurry increases dissipation rate of energy and power draw growth as a result. On other hand, higher viscosity hinders rise velocity of gas bubbles that leads to higher gas hold up almost twice up to 1.35% (Figure 8). Being small the bubbles follow the flow of the primary phase. The flow pattern of the radial impeller has two loops

Flow type		Torque, mN·m	
		Experimental	CFD
Single phase	CMC 50000 (0.15 w %)	68 ± 3	65.6
	Thiosulphate slurry	-	103.0
Multiphase	Thiosulphate slurry	-	101.2

Table 6: Simulated VS experimental torque.

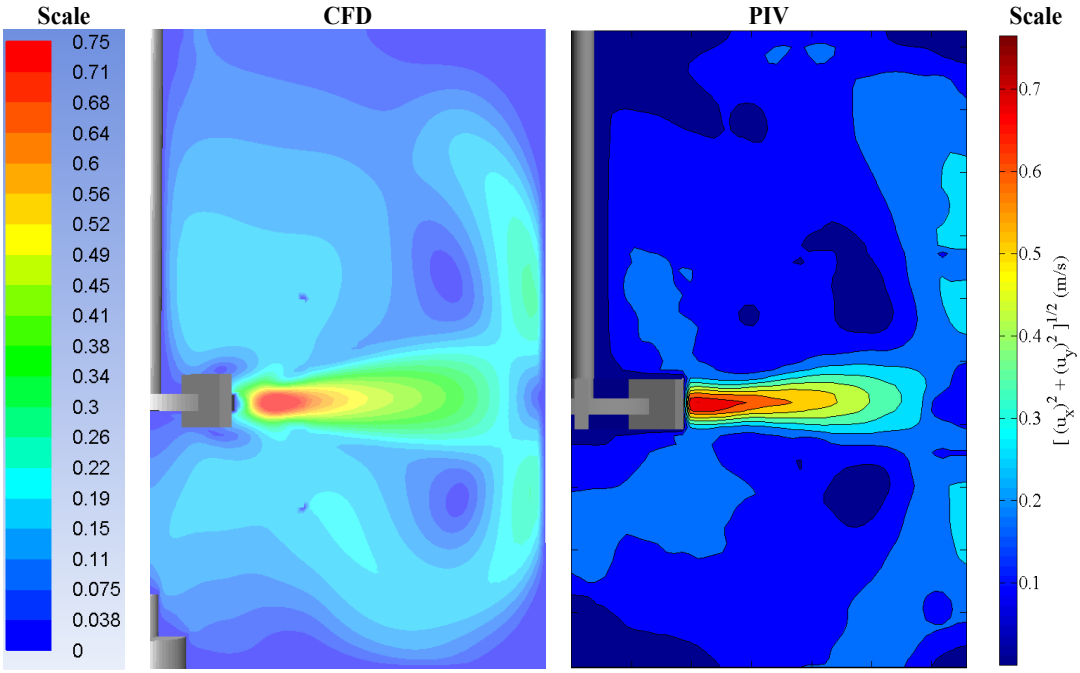

Figure 15: Average velocity field contours of water-based CMC 50000 (0.15 %) mixing at 6.67 rps modeled by CFD and measured by PIV.

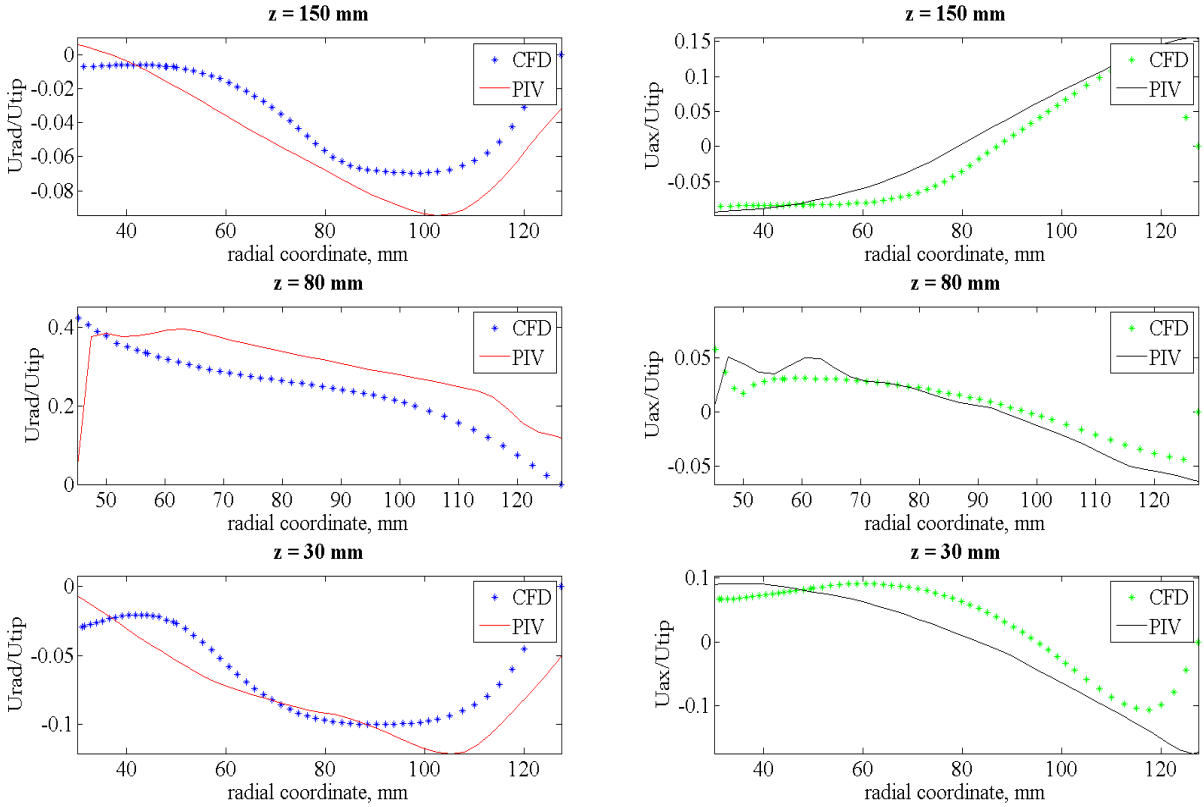

Figure 16: Comparison of normalized mean velocity components, measured by PIV and simulated by CFD of water-based CMC 50000 (0.15 %) mixing at 400 rpm, sampled at different vertical positions.

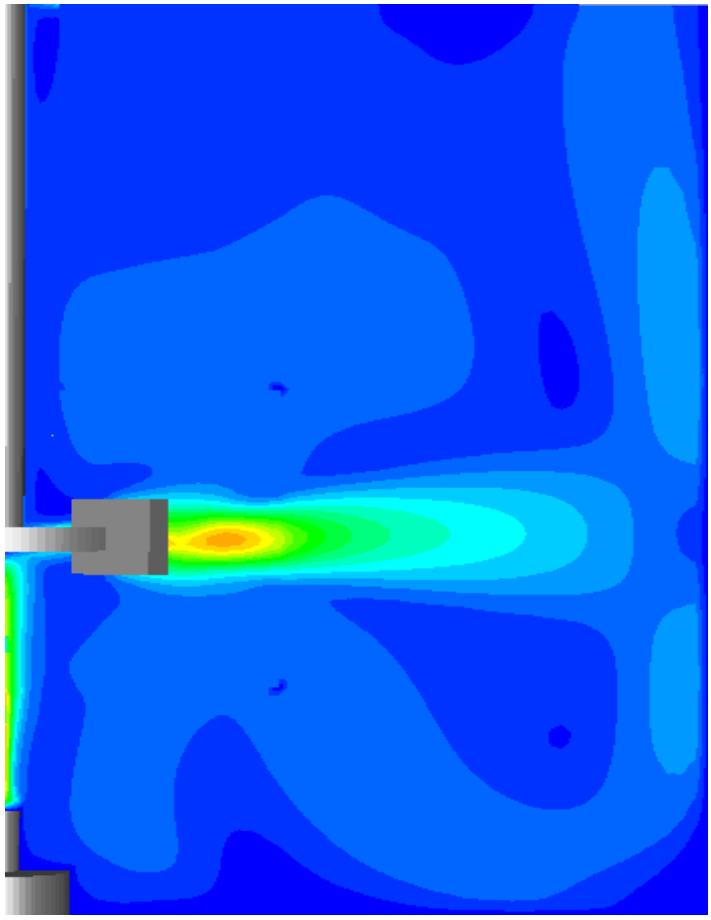

Figure 17: Average velocity contour fields of the slurry mixed at 400 rpm and aerated at 1.25 L/min (d_b=1.5 mm).

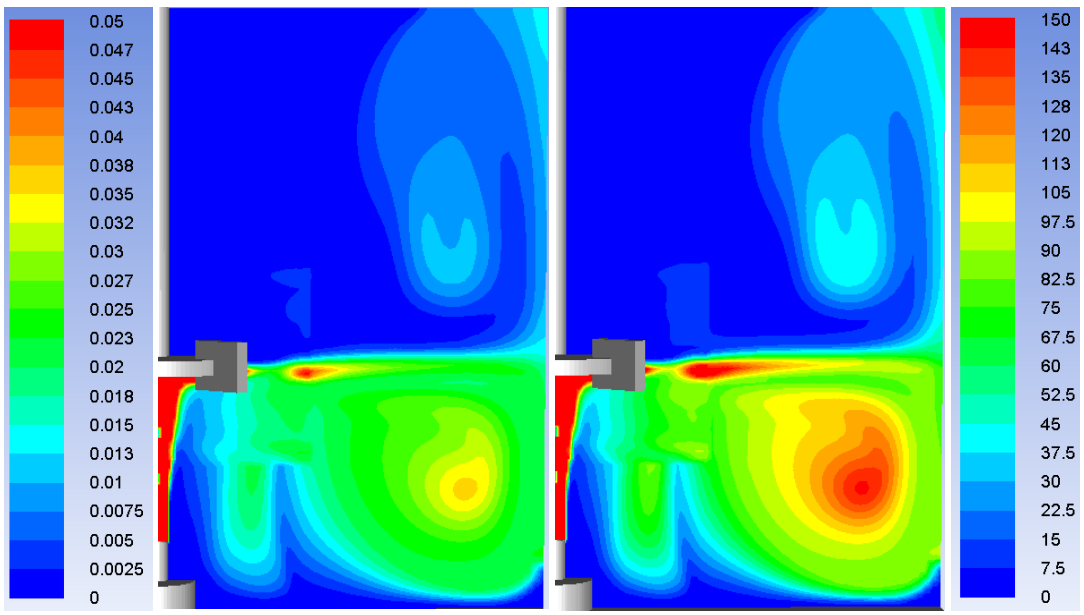

Figure 18: Contour of air volume fraction and specific surface area of the slurry mixed at 400 rpm and aerated at 1.25 L/min (d_b = 1.5mm).

of circulation. Following radial jet-flow of Rushton turbine they are dragged into down circulation while only small portion of gas goes up. The upper loop can also be distinguished since some amount of air bubbles are accumulated there. Total interfacial area is 0.26 m^2.

Mass transfer: Mass transfer has been modeled using Eq. 2. Diffusivity of oxygen in liquid depends on physical properties of solution. According to Hung and Dinius [46] increase of electrolytes concentration drops oxygen diffusivity. Diffusion coefficient of oxygen was calculated based on measured values of $D_L(O_2)$ in water with presence of sodium sulphate. Linear interpolation from the above mentioned work resulted in $D_L(O_2)=1.65 \times 10^{-9}$ m^2/s. Influence of suspended solids interaction with gas bubbles onto diffusion coefficient is unknown and neglected in this work since particles are finely milled. Theoretically, tiny particles can partially cover gas-liquid interface and cause some decrease of oxygen mass transfer into the liquid phase. However, overall k_La reduction should not be significant since interfacial area was increased drastically due to small bubbles. The distributions of specific volumetric mass transfer coefficient and mass transfer rate of oxygen are presented in Figure 19.

As it can be noticed from the distribution of specific mass transfer, the rate of mass transfer is higher in the regions where gas hold-up and energy dissipation rate are high. Therefore, the most intensive mass transfer is in the radial jet created by Rushton turbine. However, high gas hold-up of small bubbles, which do not coalesce, in the lower loop promotes mass transfer. Also, the region of moderate k_La value, caused by bubble retention in the upper circulating loop can be seen. Overall simulated mass transfer in mixed thiosulphate slurry is 0.0183 s^{-1}, which is 30% higher compared to the mass transfer measured in the mixed CMC 50000 (0.15%) solution under analogous operational conditions [47,48].

Conclusions

During this work mixing of aerated slurry on the example of thiosulphate leaching has been studied experimentally and simulated numerically. Rheology of the suspended solids was measured and found similar to those of shear-thinning fluids, which can be described by power-law model. Therefore, the slurry was imitated with water-based Carboxy Methyl Cellulose solutions (CMC 30 and CMC 50000) in order to study mixing hydrodynamics experimentally. Velocity vectors and shear rate fields of CMC 50000 (0.15 w%), mixed at 400 rpm were measured by stereoscopic PIV in vertical 2D plane.

Volumetric mass transfer was measured by dynamic method in the CMC solutions over the range of operational conditions in absence and presence of electrolytes. Presence of electrolytes promotes mass transfer of oxygen. Electrolytes decrease viscosity by breaking molecular chains of CMC that increases mass transfer coefficient. Bubbles coalescence blockage causes significant growth of surface area. Measurements of volumetric mass transfer at constant operational conditions were made with stepwise addition of electrolytes. The study revealed that decrease of bubble size is dominating factor upon k_La because viscosity drop takes place at lower salt amount. When level of electrolytes saturation is reached slight decrease of mass transfer was found at stable power draw. It could be due to contamination of the gas-liquid interfacial area.

Local gas hold-up in the aerated CMC 50000 (0.15 w%) solution was measured by EIT. Potentially the technique is capable to measure local gas hold-up in slurry. However, the sensitivity of the set-up was not enough to measure gas hold-up distribution of dispersed phase in electrolyte solution accurately.

The achieved experimental data was used in CFD modelling of the aerated slurry. Single phase non-Newtonian fluid mixing, modelled via effective viscosity, was validated against the PIV measurements of velocity components in vertical plane. Simulated and measured power consumptions of the CMC mixing at 400 rpm were in reasonable agreement. In the presence of electrolytes (0.1 mol/L) the bubble size in the CMC solution (400 rpm and 1.25 L/min) was found to be almost constant (1.5 mm). Multiphase mixing hydrodynamics of the thiosulphate slurry was modeled at the assumption of constant bubble size. Results of the simulation were presented and discussed. The simulated k_La in the leaching pulp was compared to the measured one

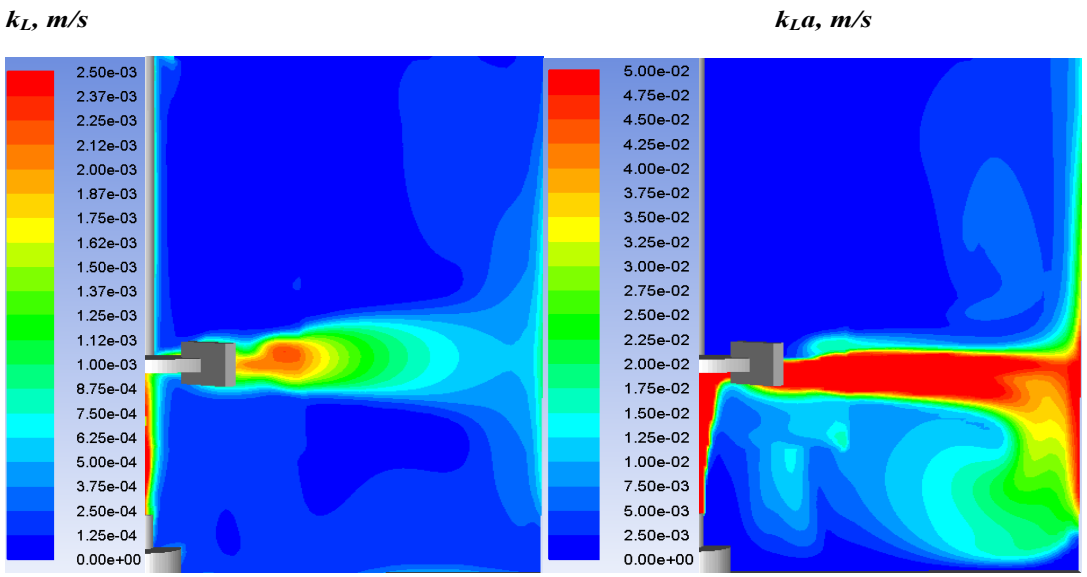

Figure19: Mass transfer coefficient and mass transfer rate of the slurry mixed at 400 rpm and aerated at 1.25 L/min (d_b = 1.5mm).

in CMC 50000 (0.15 w%) under analogous operating conditions. It was found that bigger density of the leaching slurry caused higher global gas hold-up and hence oxygen mass transfer rate [49].

Acknowledgements

The authors are grateful to the Finnish Funding Agency TEKES and, in particular, to Outotec Finland Oy collaborating under FERMATRA project (908/31/2016 and 958/31/2016), for active supervision and financial support. Also, the work of Marko Vauhkonen and Gerardo González was supported by the Academy of Finland (Project 250215 Finnish Center of Excellence in Inverse Problems Research).

Nomenclature

Symbols	Meaning	Units
A	Signal amplitude	-
A_i	Interphase surface area	m^2
C_i	Empirical coefficient	-
C_D	Drag force coefficient	-
c_{gas}	Oxygen concentration in gas phase	mol/m^3
c_{liquid}	Oxygen concentration in liquid phase	mol/m^3
d_b	Bubble diameter	m
D_L	Diffusivity in liquid phase	m^2/s
$\vec{F}_i$	Force	N
h_{gassed}	Surface level in gassed reactor	m
$h_{ungassed}$	Surface level in non-gassed reactor	m
K	Consistency index	$Pa \cdot s^n$
K_{pq}	Interphase exchange coefficient	-
k	Turbulence kinetic energy	m^2/s^2
k_L	Mass transfer coefficient in liquid phase	m/s
k_La	Volumetric mass transfer coefficient	s^{-1}
N_{fine}	Number of cells in fine grid	-
N_{coarse}	Number of cells in coarse grid	-
n	Dimensionless flow behavior index	-
NRMSE	Normalized root mean square error	%
$\overline{p}$	Pressure	Pa
P^*	Order of discretization	-
Re	Reynold's number	-
St	Stoke's number	-
T_L	Turbulence length scale	m
t	Time	s
U_T	Particle terminal velocity in turbulent flow	m/s
U_S	Particle terminal velocity in stagnant flow	m/s
$\overline{u}$	Mean velocity	m/s
u_r	Radial velocity component	m/s
u_z	Axial velocity component	m/s
V	Volume of reactor	m^3
v_{image}	Imaginary part of measured voltage	V
v_{real}	Real part of measured voltage	V

Greek letters	Meaning	Units
α_i	Phase volume fraction	-
ε	Turbulence kinetic energy dissipation rate	m^2/s^3
ε_{EIT}	Global gas hold-up measured by EIT	-
$\varepsilon_{\Delta h}$	Global gas hold-up measured by level differencing	-
$\varepsilon_{i,EIT}$	Local gas hold-up in element i, measured by EIT	-
μ	Dynamic viscosity	Pa·s
μ_{eff}	Effective viscosity	Pa·s
μ_{turb}	Turbulent viscosity	Pa·s
η	Turbulence modification factor for drag force	-
ρ	Density	kg/m^3
σ_1	Conductivity distribution of non-gassed mixing	S/m
σ_2	Conductivity distribution of gas-liquid mixing	S/m
τ	Time constant	s
τ_b	Relaxation time of bubble	s
τ_q	Relaxation time of primary phase	s
ν	Kinematic viscosity	m^2/s
γ	Shear rate	s^{-1}
λ	Kolmogorov length scale	m
φ	Signal phase	-
ϕ_i	Prediction of property value on grid i	-

Acronyms	Transcript
CCD	Charged-Couple Device
CFD	Computational Fluid Dynamics
CISTR	Continuous Ideally Stirred-Tank Reactor
CMC	Carboxy Methyl Cellulose
FEM	Finite Element Method
HWA	Hot Wire Anemometry
LDA	Laser Doppler Anemometry
MCR	Modular Compact Rheometer
Nd:Yag	Neodymium-doped yttrium aluminum garnet
PIV	Particle Image Velocimetry
UDV	Ultrasonic Doppler Anemometry
vvm	Volume of gas per volume of mixed solution per minute

References

1. Jiang T, Chen J, Xu S (1993) A kinetic study of gold leaching with thiosulfate. Hydrometallurgy, Fundamentals, Technology and Innovations. AIME, pp: 119-126.
2. Chen J, Deng T, Zhu G, Zhao J (1996) Leaching and recovery of gold in thiosulfate based system research summary at ICM. Transactions of Indian Institute of Metallurgy 49: 841-884.
3. Naito K, Sheh C, Okabe T (1970) The chemical behaviour of low valence sulfur compounds. Decomposition and oxidation of tetrathionate in aqueous ammonia solution. Bulletin of the Chemical Society of Japan 43: 1372-1376.
4. Groose AC, Dicinoski GW, Shaw MJ, Haddad PR (2003) Leaching and recovery of gold using ammoniacal thiosulfate leach liquors (a review). Hydrometallurgy 69: 1-21.
5. Joshi JB, Nere NK, Rane CV, Murthy BN, Mathpati CS, et al. (2013). CFD simulation of stirred tanks: comparison of turbulence models. Part II: axial flow impellers, multiple impellers and multiphase dispersions. Canadian Journal of Chemical Engineering 89: 754-816.
6. Jensen K (2004) Flow measurements. 10th Brazilian Congress of Thermal Sciences and Engineering 26: 400-419.
7. Khopkar A, Aubin J, Rubio-Atoche C, Xuereb C, Le Sauze N, et. al. (2004) Flow Generated by Radial Flow Impellers: PIV Measurements and CFD Simulations. International Journal of Chemical Reactor Engineering 2: 1-14.
8. Moilanen P (2009) Modelling gas-liquid flow and local mass transfer in stirred tanks. Helsinki, PhD, Finland: Helsinki University of Technology.
9. Xinhong L, Yuyun B, Zhipeng LI, Zhengming G (2010) Analysis of turbulence structure in the stirred tank with a deep hollow blade disc turbine by time-resolved PIV. Fluid Flow and Transport Phenomena 18: 588-599.
10. Busciglio A, Grisafi F, Scargiali F, Brucato A (2013) On the measurement of local gas hold-up, interfacial area and bubble size distribution in gas-liquid contactors via light sheet and image analysis: Imaging technique and experimental results. Chemical Engineering Science 102: 551-566.
11. Takeda Y (1986) Velocity Measurement by Ultrasonic Doppler Shift Method. International Journal Heat and Fluid Flow 7: 313-318.
12. Mann R, Dickin FJ, Wang M, Dyakowski T, Williams RA, et. al. (1997) Application of electrical resistance tomography to interrogate mixing process at plant scale. Chemical Engineering Science 52: 2087-2097.

13. Wang M, Dorward A, Vlaev D, Mann R (2000) Measurements of gas-liquid mixing in a stirred vessel using electrical resistance tomography (EIT). Chemical Engineering Journal 46: 93-98.

14. Kourunen J, Niiti T, Heikkinen LM (2011) Application of three-dimensional electrical resistance tomography to characterize gas hold-up distribution in laboratory flotation cell. Minerals Engineering 24: 1677-1686.

15. Arizmendi-Morquecho AM, Perez-Garibay R, Uribe-Salas A, Nava-Alonso F (2002) On-line solids hold-up measurement in mineral slurries by the standard addition method. Minerals Engineering 15: 61-64.

16. Gomez CO, Finch JA (2007) Gas dispersion measurements in flotation cells. International Journal of Mineral Processing 84: 51-58.

17. Higbie R (1935) The rate of absorption of a pure gas into a still liquid during short periods of exposure. Institution of Chemical Engineers 35: 36-60.

18. Kawase Y, Halard B, Moo-Young M (1992) Liquid-phase mass transfer coefficients in bioreactors. Biotechnology and Bioengineering 93: 1133-1140.

19. Garcia-Ochoa F, Gomez E (2004) Theoretical prediction of gas-liquid mass transfer coefficient, specific area and hold-up in sparged stirred tanks. Chemical Engineering Science 59: 2489-2501.

20. Lampinen M, Laari A, Turunen I (2015) Ammoniacal thiosulfate leaching of pressure oxidized sulfide gold concentrate with low reagent consumption. Hydrometallurgy 151: 1-9.

21. Sharikov FY, Zhukov VV, Lampinen M (2012) Investigation of Gold Oxidized Leaching Process from Concentrate of Base Ore by Utilization Calve Calorimetry. Problem Definition and First Results, Material Investigation by Utilization Methods of Thermal Analysis, Calorimetry and Gas Trapping. International Conference Reports. Saint-Petersburg: Poltorak: 59-61.

22. Wuestenberg T (2014) Cellulose and Cellulose Derivatives in the Food Industry: Fundamentals and Applications. Germany: Wiley-VCH.

23. Kourunen J (2009) Imaging of Mixing in Selelcted Industrial Processes Using Electrical Resistance Tomography. Kuopio, PhD Thesis, Finland: University of Eastern Finland.

24. Heikkinen L (2005) Statistical Estimation Methods for Electrical Process Tomography. Kuopio, PhD Thesis, Finland: University of Kuopio.

25. Holden PJ, Wang M, Mann R, Dicki FJ, Edwards RB (1999) On Detecting Mixing Pathologies Inside a Stirred Vessel Using Electrical Resistance Tomography. Chemical Engineering Research and Design 77: 709-712.

26. Tarkiff MS, Hamzah AA, Karnarudin SK, Abdullah J (2009) Electrical Resistance Tomography Investigation of Gas Dispersion in Gas-Liquid Mixing in an Agitated Vessel. Journal of Applied Science 9: 3110-3115.

27. Bawadi A, Chirag D, Nguyen T, Cooper CG, Adesoji AA (2011) Electrical resistance tomography-assisted analysis of dispersed phase hold-up in a gas-inducing mechanically stirred vessel. Chemical Engineering Science 66: 5648-5662.

28. Montante G, Paglianti A (2015) Gas hold-up distribution and mixing time in gas-liquid stirred tanks. Chemical Engineering Journal 279: 648-658.

29. Adrian R (2011) Bibliography of particle image velocimetry using imaging methods: 1917 - 1995. University of Illinois. Illinois: TAM Report 817.

30. Haario H (1994) MODEST User's guide. ProfMath Oy, Helsinki, Finland.

31. Van't Riet K (1979) Review of measuring methods and results in non-viscous gas-liquid mass transfer in stirred tanks. Industrial and Engineering Chemistry Process Design and Development 18: 357-364.

32. Ruchti G, Dunn IJ, Bourne JR (1981) Comparison of dynamic oxygen electrode methods for the measurement of kLa. Biotechnology and Bioengineering 23: 277-290.

33. Bhutani G, Cilliers JJ, Brito-Parada PR (2017) A three-dimensional numerical framework for the modeling of the pulp phase in froth flotation Computational Modeling 17: 1-8.

34. Gradov DV, Laari A, Turunen I, Koiranen T (2016) Experimentally Validated CFD Model for Gas-Liquid Flow in a Round-Bottom Stirred Tank Equipped with Rushton Turbine. International Journal of Chemical Reactor Engineering 15: 1-20.

35. Holden J (1955) Fundamentals of the hydrodynamics mechanism of splitting in dispersion processes. American Institute of Chemical Engineers Journal 289-295.

36. Schiller L, Naumann Z (1935) A Drag Coefficient Correlation. Z. Ver. Deutsch. Ing 77: 318-320.

37. Brucato A, Grisafi F, Montante G (1998) Particle drag coefficients in turbulent fluids. Chemical Engineering Science 53: 3295-3314.

38. Scot Blair GW (1939) An Introduction to Industrial Rheology. Journal of Physical Chemistry 43: 853 - 864.

39. Rewatkar VB, Deshpande AJ, Pandit AB, Joshi JB (1993) Gas hold-up behaviour of mechanically agitated gas-liquid reactors using pitched blade down flow turbines. Canadian Journal of Chemical Engineering 71: 226-237.

40. Kraume M, Zehner P (2001) Experience with Experimental Standards for Measurements of Various Parameters in Stirred Tanks. Chemical Engineering Research and Design 79: 811-818.

41. Laakkonen M (2006) Development and Validation of Mass Transfer Models for the Design of Agitated Gas-Liquid Reactors. Helsinki, PhD, Finland: Helsinki University of Technology.

42. Prince MJ, Blanch HW (1990) Transition Electrolyte Concentration for Bubble Coalescence. American Institute of Chemical Engineers Journal 36: 1425-1429.

43. Wang H, Zhai Z (2012) Analyzing grid independency and numerical viscosity of computational fluid dynamics for indoor environment applications. Building and Environment 52: 107-118.

44. Lee KC, Yianneskis M (1998) Turbulence Properties of the Impeller Stream of a Rushton Turbine. American Institute of Chemical Engineering 44: 13-24.

45. Fentiman NJ, Lee KC, Paul GR, Yianneskis M (1999) On the trailing vortices around hydrofoil impeller blades. Chemical Engineering Research and Design 77: 731-740.

46. Hung GW, Dinius RH (1972) Diffusivity of oxygen in electrolyte solutions. Journal of Chemical & Engineering Data 17: 449-451.

47. Busciglion A, Grisafi F, Montante G (1998) Particle drag coefficients in turbulent fluids. Chemical Engineering Science 53: 3295-3314.

48. Hugo P, Steinbach J (1986) A comparison of the limits of safe operation of a SBR and a CSTR. Chemical Engineering Science 41: 1081-1087.

49. Lasa HI (1986) Chemical Reactor Design and Technology. Ontario, Canada: University of Western Ontario.